SAND2021-15566C

Comparison of simulated and measured wake behavior in stable and neutral atmospheric conditions

Lawrence C. Cheung* and Myra L. Blaylock†
Sandia National Laboratories, Livermore, CA 94550, USA

Kenneth A. Brown‡, James Cutler§, Nathaniel B. deVelder¶, Thomas G. Herges‖,
Alan S. Hsieh**, and David C. Maniaci††
Sandia National Laboratories, Albuquerque, NM 87185, USA

In this study we performed detailed comparisons of numerical computations of single turbine wakes with measured data under neutral and stable atmospheric stability conditions. LES of the ABL inflow and turbine wakes are carried out using the ExaWind/Nalu-Wind simulation codes and compared with the equivalent measurements from the SWiFT research facility at wind speeds of 8.7 m/s and 4.8 m/s. The computed ABL inflow profiles and spectra showed good agreement with measured data in both stratification conditions, and the simulated turbine power and rotor speed also agreed with the measured turbine performance. A comparison of the downstream wake deficit profiles and turbulence distributions with lidar observations also showed that the LES computations generally captured the wake evolution in both neutral and stable conditions, with some possible discrepancies due to uncertainty around the turbine thrust and yaw settings. Finally, an examination of the downstream turbulence spectra showed that the peak frequency of the wake added turbulence corresponds to the characteristic wake shedding frequency, and we show that the turbulent integral lengthscale in the wake region also decreases significantly due to the presence of smaller turbulent features.

I. Introduction

The recent growth of renewable energy and wind farm sizes and has placed a new emphasis on understanding the interactions between the atmospheric inflow and wind turbine wakes. While turbine designs often consider a range of different atmospheric boundary layer (ABL) properties, such as wind profile, shear, and turbulence, the presence of turbine wakes can drastically change the conditions for downstream wind turbines. Understanding the magnitude of these changes is critical to maximizing the power extraction possible and minimizing the turbine loads experienced by the wind farm as a whole.

Previous studies [1–3] have indicated that atmospheric stability has a strong impact on downstream wake behavior. Lidar wake measurements of an onshore farm by Zhan et al [1] found that atmospheric stability noticeably affected the far wake evolution and recovery, while not strongly impacting the near wake behavior. Similarly, Dörenkämper et al [2] found stronger stable ABL wake effects in offshore wind farms compared to neutral or convective conditions, which was possible due to the decreased momentum flux in the presence of stable stratification.

A number of semi-empirical and computational methods are available to study the behavior of wakes under varying atmospheric conditions. Semi-empirical models, such as the Jensen [4] or Frandsen [5] models, provide a fast estimate of the wake deficit and wake turbulence. However, the validity of semi-empirical models depends heavily on the conditions used for calibration, and may not cover the full range of stratified conditions. On the other hand, high fidelity numerical computations such as Large Eddy Simulations (LES) are able to capture all relevant atmospheric phenomena without the need to calibrate wake behaviors. LES studies have been previously used for studying atmospheric stability [6, 7], as well as turbine performance and wakes [8–10]. However, a comprehensive comparison of LES computed,

*Principal member of technical staff, Thermal/Fluid Sciences & Engineering Dept., AIAA Member
†Principal member of technical staff, Thermal/Fluid Sciences & Engineering Dept., AIAA Member
‡Senior member of technical staff, Wind Energy Technologies Department, AIAA member
§Research assistant, Wind Energy Technologies Department, AIAA member
¶Postdoctoral appointee, Wind Energy Technologies Department, AIAA member
‖Senior member of technical staff, Wind Energy Technologies Department, AIAA member
**Senior member of technical staff, Wind Energy Technologies Department, AIAA member
††Principal member of technical staff, Wind Energy Technologies Department, AIAA member

Table 1 Measured neutral and stable atmospheric conditions at the SWiFT site.

Stability	Hub-height Wind Speed	Shear α	TI
Neutral	8.69 m/s	0.14	0.108
Stable	4.75 m/s	0.50	0.034

stratified wakes with experimental data has not been fully investigated to date. In addition, a detailed examination of the turbulence within the turbine wake region, including the characteristics of the wake-added turbulence, has not yet been documented. Understanding the nature of the wake added turbulence in the presence of atmospheric stratification is a critical element to developing models for loads in downstream turbine rows of wind farms.

In the current study, we focus on detailed comparisons of numerical computations of single turbine wakes with measured data under neutral and stable atmospheric stability conditions. LES of the ABL inflow and turbine wakes are performed using the ExaWind simulation codes and compared with the equivalent measurements from the SWiFT research facility. The ABL inflow characteristics are compared between the simulated and measured cases, along with selected turbine performance metrics. Using the available lidar measurements, the mean wake properties are compared against the LES results. Finally, we examine the same wake turbulence characteristics, such as the wake spectra and turbulent lengthscale from the simulated results.

II. Methodology

A. SWiFT measurements

The Scaled Wind Farm Technology (SWiFT) facility [11, 12], built by Sandia National Laboratories, has been used to study wake interactions between turbines. It is a highly-instrumented wind turbine test site located at Texas Tech University's National Wind Institute Research Center in Lubbock, Texas, and is targeted at acquiring high-fidelity data required for the validation of atmospheric and turbine simulations [13].

The SWiFT facility includes two instrumented meteorological towers with sonic anemometers at five heights (10 m, 18 m, 32 m, 45 m, and 59 m above the ground) and three research turbines instrumented with strain measurements, rotor azimuth and yaw angle sensors, and nacelle accelerometers. The research turbines are modified Vestas V27 turbines with a hub height of 32.1 m and a rotor diameter of 27 m.

In addition to the atmospheric and turbine measurements, the SWiFT facility also includes customized scanning lidar measurements from the Technical University of Denmark (DTU) to measure the detailed location and strength of the turbine wake at several distances downstream. The continuous-wave, DTU SpinnerLidar was nacelle mounted and rear facing, acquiring 984 line-of-sight velocity measurements in a rosette pattern across a spherical surface during each 2 second scan. Each scan had a fixed focus distance. The lidar scan configuration changed throughout the field campaign to both capture wake evolution over multiple focus distances and wake dynamics concentrating at one focus distance. The SpinnerLidar data was quality assured and quality controlled (QA/QC) according to [14]. The reader is referred to [10, 15] for more details on the lidar setup, processing, and uncertainty.

From measurements gathered at the SWiFT facility in June and July 2017, two ABL conditions were selected for simulations. To arrive at each condition, data from six different 10-minute averages with similar stability characteristics was ensemble averaged. As shown in Table 1, the two averaged cases were a neutral ABL condition with 8.7 m/s wind speed and a stable ABL condition at 4.8 m/s wind speed, matching the neutral and stable conditions discussed in [9]. As expected, the stable ABL condition is associated with much stronger wind shear and lower turbulence values, which will subsequently impact the wake evolution and wake turbulence when compared to the neutral ABL condition. However, note that the stable condition selected here also contained much less veer than typical stably stratified conditions, which allows for better comparisons of downstream wake profiles without the effect of wake skew. As will be discussed below, the stable case also contained a moderate mean yaw offset.

In the current study, we will primarily focus on the wake behavior from the leading turbines, and not on the wake interactions with downstream turbines. Details on the modeling approach for the leading turbine and its wake behavior are discussed in the following sections.

Table 2 Simulated domain sizes and grid sizes used in the LES computations.

Stability	Domain size	Background Δ	Refined Δ	z_0	temperature gradient
Neutral	4 km $\times$ 4 km $\times$ 1 km	10m	0.3125m	0.01m	0 K/hr
Stable	1.5 km $\times$ 0.75 km $\times$ 1 km	5m	0.3125m	0.0025m	-1.0 K/hr

B. Simulation

1. Nalu-Wind precursor and turbine simulations

The simulations in the current work are performed using the ExaWind/Nalu-Wind LES flow solver coupled with OpenFAST* to model the aero-elastic behavior of the wind turbine. The Nalu-Wind solver [16, 17] is based on an unstructured, finite volume approach to solve the incompressible Navier-Stokes equations with a low-Mach number approximation. Both the Coriolis forcing and Boussinesq bouyancy model can be included to capture the effects of wind veer and atmospheric stratification. In all simulations, the subgrid-scale kinetic energy one-equation turbulence model was used for turbulence closure. At the lower boundary, the sub-filter scale stresses are applied following the formulation of [18]. Nalu-Wind has been previously used to model the Cape Wind offshore ABL under various atmospheric conditions [6, 7], as well as for turbine wake studies in onshore wind farms [8–10], and more details on the implementation of the flow solver can be found in the cited references.

The domain and mesh sizes used in the neutral and stable simulations are summarized in table 2. Both simulations used a 1 km vertical domain, however, a larger 4 km $\times$ 4 km horizontal domain was used for the neutral ABL compared to the 1.5 km $\times$ 0.75 km for the stable domain. This difference in domain size is due to the expected dependence of the turbulent lengthscale on atmospheric stratification. In the neutral ABL case, the larger domain allows for the longer turbulent structures to develop and evolve, while the smaller domain was adequate for the smaller-scale turbulent structures in the stable ABL case. To resolve the smaller-scale turbulent eddies, though, the stable ABL case required a finer resolution background mesh than the neutral, which lead to a slightly larger overall mesh size: 75.9 million elements for the stable ABL case, and 64.8 million for the neutral ABL case. In both cases, the finest mesh region near the turbine rotor used a grid size of 0.3125 m, based on the previous work of [8, 10].

The simulations for both the neutral and stable turbine wake cases were carried out in two stages. First, a set of precursor simulations were performed without any turbine models present to develop the correct inflow and turbulence characteristics in the ABL. In the second stage of the simulations, the turbine model was inserted into the domain and the wakes were allowed to develop before collecting and averaging statistics.

During the precursor stage of the simulations, periodic boundary conditions were applied in both the x and y directions. At the upper boundary, an inflow/outflow boundary condition based on a potential flow solution was applied along with specified temperature gradient. Furthermore, an inversion layer was placed at z=650m (neutral ABL) and z=450 m (stable ABL) to limit to the growth of the boundary layer. At the lower boundary, the ground was assumed to be flat with a small degree of surface roughness, and the wall model of [18] was applied. The precusor calculations also used an ABL forcing scheme where a constructed pressure gradient was applied to ensure that the hub-height wind speed matched the specified value from the SWIFT measurements. To arrive at the correct shear and turbulence intensity characteristics matching the SWIFT measurements, two wall model parameters were varied at the ground: the surface roughness z_0 and the applied temperature gradient at the ground. In the neutral ABL case, no heat flux was applied, while in the stable ABL case, a negative heat flux corresponding to a temperature gradient of -1.0 Kelvin/hour was applied (see table 2).

After the appropriate settings were determined, each case was run for a sufficiently long period of time for the inflow turbulence to evolve, and for the correct ABL statistics to develop. The neutral ABL case was run for total of 25,000 seconds, and the stable ABL case for 30,000 seconds, after which a specific time window within the last 5,000 seconds of the run was analyzed to use for the full turbine run. Time windows for the stable and neutral cases were taken to be 10 minutes and 20 minutes respectively, and were chosen based on a search algorithm that weighted results for mean wind speed, mean shear exponent, and mean turbulence intensity. Turbulence intensity is defined as

$$TI_\sigma = \frac{\sigma_U}{|U|}, \tag{1}$$

*https://nwtc.nrel.gov/OpenFAST

where U is the hub-height longitudinal wind speed at 2.5D upstream of the rotor, and σ_U is the standard deviation of U. The mean of TI_σ, as well as the other variables noted, is a single point time average over the entire time window.

2. Turbine model and simulation

Once the boundary conditions and appropriate simulation window were identified for the precursor, the full turbine and wake simulations was run in Nalu-Wind. To represent the effect of the V27 wind turbines on the ABL, a modified actuator line model was used during the turbine simulations. The actuator line model (ALM) is implemented by following [19], where the fluid-structure interaction is simulated through a body force f_i in the momentum equation of the form

$$f_i = \int_0^L F_i(l) g(\mathbf{r})\, \mathrm{d}l \tag{2}$$

where l is the distance along an actuator line and F_i is the actuator line force computed from the incoming velocity flow and the airfoil characteristics specified in OpenFAST. The smoothing kernel $g(r)$ has the form

$$g(r) = \frac{1}{\epsilon \pi^{3/2}} \exp\left(-\frac{r^2}{\epsilon^2}\right) \tag{3}$$

where ϵ is a characteristic length scale that determines the volume over which the body forces are spread.

The application of the Filtered Lifting Line Correction (FLLC) to the actuator line model is described in detail in [20]. Like the traditional ALM model, it first computes the forces from the aerodynamic model of the blade. It then calculates the gradient of the lift distribution along the blade. The induced velocity from the gradient of the lift is found using both a specified epsilon and also for an optimum ϵ. In this case we set the optimal value of epsilon to be one-quarter of the chord length along the blade, which was shown in [21, 22] to give the correct value for power. The specified minimum epsilon was set to 0.625 m to match twice the grid spacing. A velocity correction term is set to be the difference between these two induced velocities. The forces for the actuator line are then computed using the induced velocities plus this correction term.

For both the neutral and stable ABL cases, the same turbine parameter settings and similar simulation settings were used. The timestep in both cases was Δt=0.01 s, although the neutral ABL case was run to ensure that 20 minutes of statistics could be gathered past the initialization phase, while the stable ABL run was run to collect only 10 minutes of flow statistics. Also, to mimic the low-veer conditions under which the stable ABL wake data was collected, the Coriolis forcing was removed from both the stable precursor and turbine runs, while it remained active for the neutral simulations.

III. Results

From the simulation results, an initial qualitative view of the simulated ABL inflow and turbine wakes can be seen in figures 1 and 2. Figure 1 shows instantaneous contours of the ratio of horizontal velocities $U_{turbine}/U_{precursor}$ for both the neutral and stable ABL cases. In these images, the higher inflow turbulence and larger amplitude wake meandering of the neutral ABL simulations is immediately visible when compared to the stable simulations. The longer wake persistence and larger downstream wake deficit of the stable case is also evident. A more detailed view of the turbine tip vortex structure is shown in figure 2, where isosurfaces of the q-criteria can also be used to highlight the differences in wake behavior. In the neutral ABL simulations, we observe that the interaction of the inflow turbulence with the turbine wake leads to a faster breakdown of the tip vortices within a few diameters downstream of the turbine location. On the other hand, the lower ambient TI conditions for the stable ABL case interact with the wake to smaller degree, allowing the tip vortices to remain well-organized much farther downstream.

In the following sections we provide a more detailed, quantitative discussion of the incoming ABL flow and the turbine wake differences. First, in section III.A, the simulated inflow profiles and spectra are compared with corresponding SWiFT measurements, followed by a comparison of specific turbine quantities in section III.B. Finally, an exploration of the differences in wake profiles and turbulence characteristics is presented in section III.C.

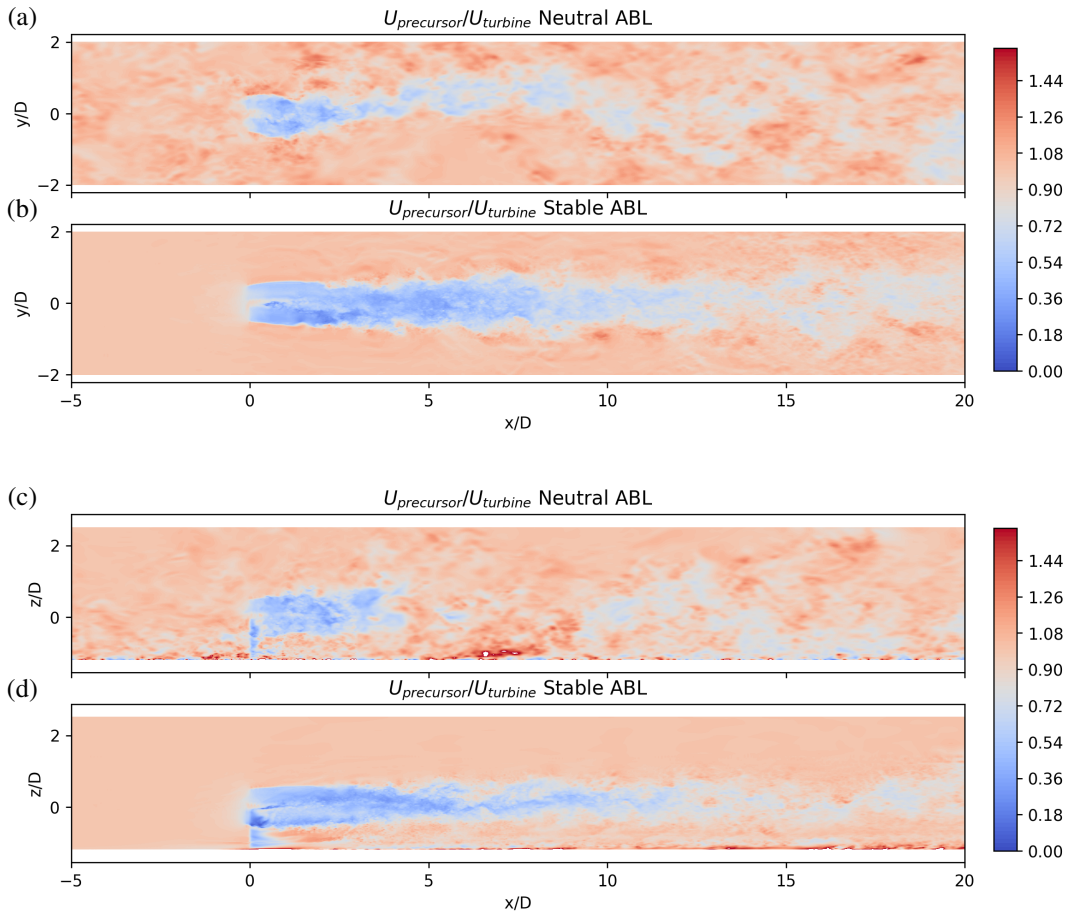

Fig. 1 Comparison of the instantaneous wake deficit $U_{turbine}/U_{precursor}$ at t=200s for the neutral and stable LES computations. Top down, hub-height view for (a) neutral and (b) stable ABL, and side view for (c) neutral and (d) stable ABL.

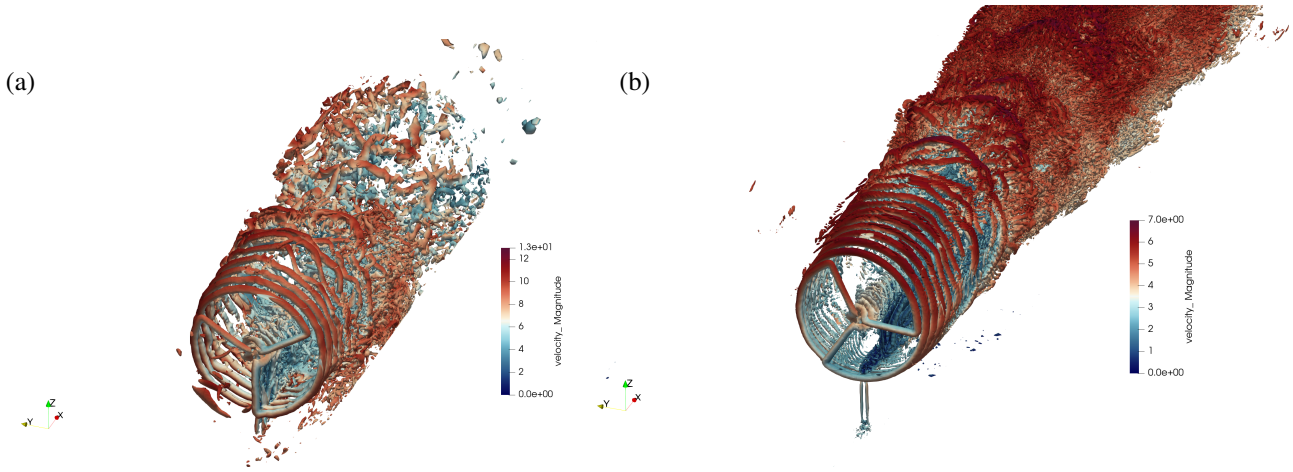

Fig. 2 Tip vortex visualizations of q-criteria highlighted by velocity magnitude for the (a) neutral ABL simulation and (b) stable ABL simulation

A. Inflow profiles and wind spectra

ABL profiles

In the Nalu-Wind simulations, a virtual met mast was included to capture the same wind speed measurements as the sonic anemometers at the SWiFT facility. The virtual met mast probes were placed at the same locations relative to the turbine and also spanned the same elevations (z=10 m to z=58 m) as the SWiFT measurements. As shown in figure 3, we found good agreement between the Nalu-Wind calculated and SWiFT measured incoming flow profiles for the neutral and the stable ABL cases. Both the hub-height wind speed and the amount of wind shear across the rotor disk heights were well captured by the LES calculations. Slight discrepancies can be seen in the comparisons at the lowest met mast location (z=10 m), but the agreement between the Nalu-Wind calculations and SWiFT measurements is still fairly close at the at highest available measurement height (z=58 m).

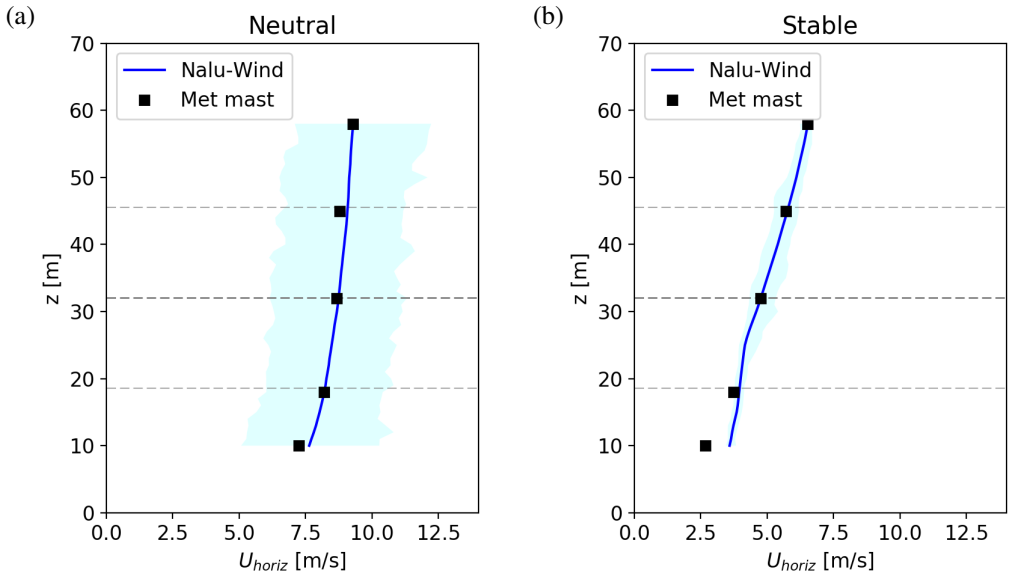

Fig. 3 Comparison of inflow wind profiles for the (a) neutral and (b) stable ABL cases, as computed by Nalu-Wind and measured by the SWiFT met mast. The shaded blue regions correspond to the minimum and maximum U_{horiz} values during the averaged time period.

Inflow wind spectra

The inflow wind spectra can also be calculated and compared using the sampled met mast velocity data from the Nalu-Wind virtual met mast and the SWiFT sonic anemometer measurements. In this work we define the single point wind spectra $S_i(f)$ as a function of the frequency f in the following manner:

$$\int_0^\infty S_i(f)\,\mathrm{d}f = \sigma_i^2, \tag{4}$$

with the indices $i = u, v, w$ denoting the longitudinal, lateral, and vertical directions respectively, and σ_i is the wind speed variance. Although the virtual met mast in Nalu-Wind was sampled at a frequency of 25 Hz, the actual maximum resolvable frequency f_{max} of the turbulence is limited by the mesh resolution in the simulation. This limit can be estimated by the expression

$$f_{max} = \frac{0.6\overline{U}}{N\Delta} \tag{5}$$

where N is number of cells required to resolve a particular wavelength (assumed here to be $N = 8$), $\overline{U}$ is mean velocity, and Δ is the mesh spacing in the flow direction. Here the turbulent eddies are assumed to convect at approximately 60%

of the mean velocity $\overline{U}$, although the exact convection speed will vary depending on frequency. The results from the Nalu-Wind simulations and SWiFT sonic anemometers can also be compared against the Kaimal model for wind spectra [23, 24]

$$\frac{fS_i}{u_\tau^2} = \frac{a_i(fz/\bar{U})}{\left(1 + b_i(fz/\bar{U})^{\alpha_i}\right)^{\beta_i}} \tag{6}$$

which was developed and calibrated for neutral atmospheric conditions over flat terrain. For this study, the a_i, b_i, α_i, and β_i parameters in equation (6) are taken to be the standard constants given in Table 3.

Table 3 Parameters for Kaimal model

Direction i	a_i	b_i	α_i	β_i
Longitudinal, u	105.0	33.0	1	5/3
Lateral, v	17.0	9.5	1	5/3
Vertical, w	2.1	5.3	5/3	1

Figure 4 shows the comparison between the Nalu-Wind calculated, SWiFT measured, and Kaimal modeled wind spectra for both the neutral and stable ABL cases. In general, good agreement is seen between the LES computed spectra and the SWiFT measured spectra up to the maximum resolvable frequency f_{max}. For the stable ABL case, a stronger decrease in spectra with height z is visible, although the computed peak amplitude and peak frequency still agrees with the measured spectra. The neutral spectra shows a much weaker dependence of the spectra with height, which is also consistent with the lower shear exponent in the mean profile.

The Kaimal model spectra at the turbine hub-height also agrees well with the calculated and measured spectra in the neutral case, for all three directions. However, the stable spectra does not follow the Kaimal model predictions, as it overpredicts the low frequency amplitudes. This is consistent with previous studies on ABL spectra [7], and suggests that recalibration is necessary for the Kaimal spectra under non-neutral conditions.

B. Wind turbine performance comparison

The coupling of OpenFAST with the Nalu-Wind solver allows the simulation to replicate the operation and behavior of the Vestas V27 turbine within the flow. The outputs from the OpenFAST module, such as forces on the turbine components or turbine performance metrics, can also be averaged and compared against the measured turbine quantities from the SWiFT facility. In table 4 below, the generator power and rotor speed of the V27 has been averaged from the Nalu-Wind simulation and compared with the equivalent quantities from the SWiFT measurements. For both the neutral and stable ABL cases, these quantities agreed well with the SWiFT measurements.

Some additional turbine settings used in the Nalu-Wind simulations did not have an available experimental comparison, or were more difficult to match exactly. For instance, although the turbine thrust measurement is not available for the selected ABL conditions, the blade forces from the OpenFAST output can also be used to calculate a thrust coefficient Ct based on the rotor aerodynamic thrust forces. The averaged rotor aerodynamic Ct for the neutral and stable ABL cases was 0.73 and 0.81, respectively, and is consistent with values previously reported in [9]. Additionally, a turbine yaw of 0.0 degrees was used in both of the Nalu-Wind simulations. However, the averaged turbine data from the six measurement bins indicated that a mean turbine yaw of 1.0 degrees and 8.2 degrees for the neutral and stable ABL cases, respectively. As discussed in section III.C, this discrepancy in the turbine thrust and yaw may impact the wake profile comparisons between simulation and SWiFT data as well.

Table 4 Comparison of the calculated turbine model outputs with the observed turbine behavior from SWiFT

Case	Generator Power	Rotor speed
Nalu-Wind Neutral	79.8 kW	43.4 rpm
SWiFT Neutral	79.1 kW	42.8 rpm
Nalu-Wind Stable	14.2 kW	25.0 rpm
SWiFT Stable	13.3 kW	26.4 rpm

C. Comparisons of wake profiles and spectra

1. Wake velocity comparisons

Wake quantities of interest are compared here in the meandering frame of reference, which in some cases offers insight into model validation, as opposed to the fixed frame of reference. See Hsieh *et al*. [10] for evidence and for the procedure used for calculating the meandering frame. As introduced previously, it should be borne in mind that the measured and simulated data compared below do not capture precisely the same quantities; the lidar measures along a line of sight and includes a weighted contribution from the velocity field depending on the location of the focus distance whereas the simulation provides conventional point measurements at the locations on the plane of interest.

Figure 5 indicates that the time-averaged cross-sectional wake velocities for the experiment and simulation show good qualitative agreement in terms of wake diameter and peak wake deficit. On the other hand, several subtle differences are apparent. For both the neutral and stable cases, the simulation produces higher velocity near the origin than the experiment, which is a feature that has been observed previously in simulations using high-fidelity simulations [9, 10]. Further, the stable ABL simulation result in figure 5(d) shows the apparent the existence of perturbations in the wake that make swirl apparent that are not replicated by the measurement in figure 5(c). Given that the spatial resolution of both the lidar and LES should be sufficient to capture such swirl features, it is believed that the wake swirl signature in the experiment may be smoothed out because of the relatively greater unsteadiness in inflow wind direction for the experiment than the simulation, though the simulation's ability to capture the turbulent wake mixing is not ruled out as a culprit. Another unique feature of this stable ABL simulation case is the tower effect that is present near y/D=0 and z/D=-0.6. The absence of a pronounced tower effect in the corresponding stable experimental data is possibly an artifact of the lidar's line-of-sight weighting and its sparse spatial resolution relative to the tower thickness. For the neutral cases, the tower effect is not visible for either experiment or simulation as turbulent mixing apparently smooths over the tower deficit by the 2.5D position. It is also possible that the tower wake and wake swirl discrepancies are related to some degree, as the stronger tower wake in the simulation may be the cause of stronger observable swirl effect in the simulated wake.

Figures 6 and 7 offer a view of the wake evolution by considering horizontal and vertical slices, respectively, at different streamwise positions. In these figures, the boundary layer measured by the meteorological towers (both physical and virtual) is removed from the data to produce the wake velocity deficit, $U_D = U - U_I$, where U_I is the boundary layer inflow profile calculated with a 45 s moving average. Both the horizontal and vertical slices indicate that the jet-like flow behind the simulated nacelle described previously mixes out by the 4D position for the neutral case and by the 4-5D position for the stable case. Ignoring the jet feature in the simulated data, it appears that the shape of the wake "bucket" profiles agrees well between the 2D and 4D positions except for an offset towards higher velocity in the case of the simulation, which could be related to suspected differences in the experimental and simulated turbine thrust (especially for the neutral case where the offset is present even at the 2D position). At the 5D position, however, the shape of the wake bucket becomes less steep in the experiment than in the simulation for the neutral case (both figures 6(a) and 7(a)), which is hypothesized to be related to the larger wake meandering amplitudes in the experiment. The opposite trend is observed for the stable case at 5D (figures 6(b) and 7(b)), but the cause for this faster wake recovery in the simulation versus the experiment in the stable ABL is unclear, though we note that the difference begins to appear as the wake transitions from a near-wake to far-wake state.

2. Wake fluctuation comparisons

In addition to the comparisons of time-averaged results in the previous subsection, we here use an exploratory approach to gauge the similarity of the fluctuating behavior in the simulation compared to that in the experiment. Plotted in figure 8 is the standard deviation of simulated wake velocity (in subfigures (b) and (d)) and the mean spectral standard deviation of the distribution of velocities within the measured probe volume (in subfigures (a) and (c)). The latter quantity is considered a valid approximation of the former since the wavelength of the wake-added turbulence is generally of smaller scale than the full-width half-maximum probe length of 8.4 m at the x=2.5D position. However, the approximate nature of the comparison should be borne in mind, specifically as related to any remaining scales that are larger than the probe length and to the spatial averaging inherent in sampling over the probe length. Note also that the exclusion of the sub-grid scale from the simulated results in figure 8 is not expected to be a main source of error since the mesh refinement of the LES is relatively small at 0.625-1.125 m and 0.3125 m for the neutral and stable cases, respectively, at this location.

For the neutral case, both the experiment and simulation show a nearly axisymmetric annulus of turbulence, which

begins just inside the projected rotor diameter. The radial extent of these rings is larger for the experiment, which may be related to the larger meandering amplitudes in the experiment or to the averaging along the lidar line of sight. The simulation additionally has a region of higher unsteadiness near the origin, which appears correlated with the shear layer generated by the jet-like flow from the nacelle region referenced above. For the stable case, there is a distinct difference between the experimental and simulated results as the experiment shows only a partial annulus rather than the nearly full one in the simulation. While conclusions about this difference have not been finalized, it is suggested that the presence of the partial annulus is due to the mean yaw offset present in the experiment but not in the simulation, and that the wake swirl (clockwise from this orientation) has rotated the higher turbulence generated from the downstream half of the rotor towards the top-dead-center position. See also the left-to-right asymmetry in turbulent kinetic energy at the $3D$ wake position as reported for the yawed cases in Bartl *et al*. [26].

3. Wake spectra

While the comparisons with the lidar measurements in the previous section highlighted the spatial distribution of turbulence inside the turbine wakes, we can also quantitatively assess the amount of turbulence which is created by the wake itself. This can be achieved by comparing the undisturbed spectra from the precursor ABL calculations with the wake spectra at the same positions from the turbine LES calculations.

The results are illustrated in figures 9 and 10, where the spectra in the wake regions from both the precursor ABL calculations and the turbine calculations are shown for the heights z=32.1 m, 45.6 m, and 70 m. The spectra was also calculated at the three downstream locations x/D = 3, 5, and 7. For the three heights considered here, the wake added turbulence is most evident at the hub height (z=32.1 m) and upper rotor tip heights (45.6 m). As expected, the spectra outside the wake region, at the upper most height of z=70 m, is not impacted by the presence of the turbine, so the turbine spectra collapse agrees with the precursor spectra at all downstream distances for both neutral and stable ABL cases.

The majority of the turbulent energy increase in the turbine simulations occurs within the inertial range of the spectrum. In the neutral ABL case, the spectra associated with the wake added turbulence quickly returns to inflow precursor levels in the energy containing range of the spectra. For the stable ABL turbine run, the spectra in the energy containing range remains elevated compared to the precursor inflow spectra in the energy containing range, but the overall amplitudes are more comparable to the neutral spectra levels as predicted by the Kaimal spectra.

The frequency of the peak amplitudes for the wake added turbulence in both the neutral and stable ABL cases can be estimated by considering the characteristic wake shedding frequency. This shedding frequency is calculated via the Strouhal number St based on turbine rotor diameter D and hub-height inflow velocity U_∞:

$$\mathrm{St} = \frac{fD}{U_\infty} \tag{7}$$

In the current work, the fundamental shedding frequency f_0 is calculated assuming a Strouhal number of St=0.19, which is consistent with experimentally measured values for shedding behind bluff body objects [27, 28]. As shown in figures 9 and 10, the peak of the wake-added turbulence spectra, plotted non-dimensionally as fS_i/U_∞^2, generally peaks at either f_0 or its first harmonic $2f_0$. As expected, the spectral peak is more distinct for the stable ABL due to the absence of wake meandering and lower levels of inflow turbulence. For both neutral and stable cases, the peak in wake added turbulence is also more observable at the x=3D and 5D downstream distances, and as the wake profiles broaden, the wake spectra also broadens at x=7D.

4. Turbulent correlation and integral lengthscale

In addition to the changes in the turbulent spectra seen in the turbine wake, we can also observe the changes in the turbulent structure through the correlation tensor function and turbulent integral lengthscale. While difficult to measure experimentally, these quantities can be computed from the LES sampled flow fields, and would allow us to determine the size of the turbulent eddies both inside and outside the turbine wakes.

Here we define the two-point spatial correlation tensor function $R_{ij}(\mathbf{x}, \boldsymbol{\xi})$ at a point $\mathbf{x}$ and a separation distance $\boldsymbol{\xi}$ as

$$R_{ij}(\mathbf{x}, \boldsymbol{\xi}) = \frac{\langle u_i'(\mathbf{x}, t) u_j'(\mathbf{x} + \boldsymbol{\xi}, t) \rangle}{\sqrt{\langle u_i'^2 \rangle} \sqrt{\langle u_j'^2 \rangle}} \tag{8}$$

Table 5 Turbulent integral lengthscale L calculated from equation (10).

ABL Stability	Precursor Run	Turbine Run
Neutral	206.3 m	137.6 m
Stable	15.5 m	7.3 m

where the velocity fluctuations u_i' are defined in terms of total velocity u_i and mean velocity $\overline{u_i}$ components:

$$u_i'(\mathbf{x}, t) = u_i(\mathbf{x}, t) - \overline{u_i(\mathbf{x}, t)} \tag{9}$$

In the current work we are primarily investigating the longitudinal lengthscale with the first component R_{11}, so the turbulent integral longitudinal lengthscale L can be calculated as

$$L = \int_0^\infty R_{11}(\xi)\, \mathrm{d}\xi \tag{10}$$

where the separation vector $\boldsymbol{\xi}$ is taken to be in the streamwise direction of the flow, and $R_{11}(\xi)$ is time-averaged over the available flow field data. In practice, the upper limit on the integral in equation 10 is taken to be the location where R_{11} first vanishes, i.e., the location ξ_0 where $R_{11}(\xi_0) = 0$.

In the neutral and stable ABL simulations, the spatial correlation function $R_{11}(\xi)$ was calculated on the hub-height plane in the turbine wake region extending from the rotor location to about 14.8D and 5.5D downstream, respectively and averaged over 20 minutes and 10 minutes, respectively. The calculation of R_{11} was also performed using the same refined grid and simulation setup for the precursor and the turbine run to allow for better comparison. The behavior of $R_{11}(\xi)$ for both atmospheric stabilities and both the precursor and turbine wake runs is shown in figure 11. The calculated lengthscale L for all cases is also given in table 5. As expected, the turbulent lengthscale is an order of magnitude larger for the neutral ABL than the stable ABL. This is consistent with previous ABL integral lengthscale calculations shown by [7]. However, in the turbine calculations, the integral lengthscale in the rotor wake regions also decreased by approximately 30%-50% compared to the precursor runs.

This decrease in turbulent lengthscale is consistent with the changes in wind spectra discussed in section III.C.3 above. In the precursor inflow simulations, the turbulent lengthscale is largely determined by the large scale structures and energy containing region of the spectra. However, inside the turbine wakes, the wake added turbulence is typically at a higher frequencies and smaller scales than the inflow turbulence. In the presence of the wake added eddies, the turbulence decorrelation is accelerated, leading to shorter turbulent lengthscales.

IV. Conclusions

In the current work, we compared the turbulent inflow and wake behavior of turbines operating under neutral and stably stratified atmospheric conditions. Simulations of V27 turbines performed using the ExaWind/Nalu-Wind LES code were compared with the met mast and lidar measurements from SWiFT, and a detailed examination of the wake added turbulence was carried out.

Through these comparisons, we found that the inflow ABL profiles and spectra were well captured in the LES computations for both the neutral and stable conditions. The simulated V27 turbines in the neutral and stable ABL flows were also accurately represented, and their generated power and rotor speeds agreed well with the measured SWiFT performance data. The comparisons of the downstream wake and turbulence profiles also showed that the simulated wakes were able to qualitatively capture the general wake spreading and turbulent distribution patterns observed in the lidar measurements. However, some possible discrepancies in the wake deficit and shear distribution may be due to the uncertainty around the turbine yaw and thrust settings.

Finally, from the simulated LES wake results, we found that the peak frequency of the wake added turbulence corresponded to the characteristic wake shedding frequency of St=0.19 and its first harmonic in both stratification conditions. By computing the turbulent integral lengthscale of the flow in the wake region, we found that the smaller turbulent features in the wake decreased the longitudinal lengthscale by approximately 30%-50% in both ABL conditions.

Acknowledgments

This research was supported by the Wind Energy Technologies Office of the U.S. Department of Energy (DOE) Office of Energy Efficiency and Renewable Energy. Sandia National Laboratories is a multimission laboratory managed and operated by National Technology & Engineering Solutions of Sandia, LLC, a wholly owned subsidiary of Honeywell International Inc., for the U.S. Department of Energy's National Nuclear Security Administration under contract DE-NA0003525. The views expressed in the article do not necessarily represent the views of the U.S. Department of Energy or the United States Government.

References

[1] Zhan, L., Letizia, S., and Valerio Iungo, G., "LiDAR measurements for an onshore wind farm: Wake variability for different incoming wind speeds and atmospheric stability regimes," *Wind Energy*, Vol. 23, No. 3, 2020, pp. 501–527.

[2] Dörenkämper, M., Witha, B., Steinfeld, G., Heinemann, D., and Kühn, M., "The impact of stable atmospheric boundary layers on wind-turbine wakes within offshore wind farms," *Journal of Wind Engineering and Industrial Aerodynamics*, Vol. 144, 2015, pp. 146–153.

[3] Abkar, M., and Porté-Agel, F., "Influence of atmospheric stability on wind-turbine wakes: A large-eddy simulation study," *Physics of fluids*, Vol. 27, No. 3, 2015, p. 035104.

[4] Jensen, N., "Note on wind generator interaction.[Wakes]," 1983.

[5] Frandsen, S., "Turbulence and turbulence-generated structural loading in wind turbine clusters," 2007.

[6] Cheung, L. C., Kaul, C. M., Hsieh, A. S., Blaylock, M. L., and Churchfield, M. J., "Large-eddy simulations of the Northeastern US coastal marine boundary layer," *Journal of Physics: Conference Series*, Vol. 1618, IOP Publishing, 2020, p. 062038. https://doi.org/https://doi.org/10.1088/1742-6596/1618/6/062038.

[7] Cheung, L., Brazell, M. J., Hsieh, A., Ananthan, S., Vijayakumar, G., and deVelder, N., *Computation and comparison of the stable Northeastern US marine boundary layer*, AIAA Scitech 2021 Forum, AIAA Paper 20210-0454, January 2021. https://doi.org/10.2514/6.2021-0454.

[8] Blaylock, M. L., Houchens, B. C., Maniaci, D. C., Sakievich, P., and Knaus, R. C., "Comparison Of Field Measurements And Large Eddy Simulations Of The Scaled Wind Farm Technology (SWiFT) Site," *ASME-JSME-KSME 2019 Joint Fluids Engineering Conference*, ASME, 2019.

[9] Doubrawa, P., Quon, E. W., Martinez-Tossas, L. A., Shaler, K., Debnath, M., Hamilton, N., Herges, T. G., Maniaci, D., Kelley, C. L., Hsieh, A. S., et al., "Multimodel validation of single wakes in neutral and stratified atmospheric conditions," *Wind Energy*, Vol. 23, No. 11, 2020, pp. 2027–2055.

[10] Hsieh, A. S., Brown, K. A., deVelder, N. B., Herges, T. G., Knaus, R. C., Sakievich, P. J., Cheung, L. C., Houchens, B. C., Blaylock, M. L., and Maniaci, D. C., "High-fidelity wind farm simulation methodology with experimental validation," *Journal of Wind Engineering and Industrial Aerodynamics*, Vol. 218, 2021, p. 104754. https://doi.org/https://doi.org/10.1016/j.jweia.2021.104754, URL https://www.sciencedirect.com/science/article/pii/S0167610521002336.

[11] Kumer, V.-M., Reuder, J., Dorninger, M., Zauner, R., and Grubišić, V., "Turbulent kinetic energy estimates from profiling wind LiDAR measurements and their potential for wind energy applications," *Renewable Energy*, Vol. 99, 2016, pp. 898–910. https://doi.org/10.1016/j.renene.2016.07.014.

[12] Naughton, B., "Scaled Wind Farm Technology (SWiFT) Facility Wake Steering Experiment Instrumentation and Data Processing," Report, Sandia National Laboratories, 2017.

[13] Berg, J., Bryant, J., LeBlanc, B., Maniaci, D. C., Naughton, B., Paquette, J., Resor, B., White, J., and Kroeker, D., "Scaled Wind Farm Technology Facility Overview," *AIAA SciTech 32nd Wind Energy Symposium*, 2014.

[14] Herges, T., and Keyantuo, P., "Robust Lidar data processing and quality control methods developed for the SWiFT wake steering experiment," *Journal of Physics: Conference Series*, Vol. 1256, IOP Publishing, 2019, p. 012005.

[15] Brown, K., and Herges, T., "Residual uncertainty in processed line-of-sight returns from nacelle-mounted lidar due to spectral artifacts," *Journal of Physics: Conference Series*, Vol. 1618, 2020, p. 032052.

[16] Domino, S., "Sierra Low Mach Module: Nalu Theory Manual 1.0. SAND2015-3107W, Sandia National Laboratories, Unclassified Unlimited Release (UUR)," , 2015.

[17] Sprague, M., Ananthan, S., Vijayakumar, G., and Robinson, M., "ExaWind: A multi-fidelity modeling and simulation environment for wind energy," *J. Phys. Conf. Series*, 2020.

[18] Moeng, C.-H., "A Large-Eddy-Simulation Model for the Study of Planetary Boundary-Layer Turbulence," *Journal of the Atmospheric Sciences*, Vol. 41, No. 13, 1984, pp. 2052–2062.

[19] Sorensen, J. N., and Shen, W. Z., "Numerical modeling of wind turbine wakes," *J. Fluids Eng.*, Vol. 124, No. 2, 2002, pp. 393–399.

[20] Martínez-Tossas, L. A., and Meneveau, C., "Filtered lifting line theory and application to the actuator line model," *Journal of Fluid Mechanics*, Vol. 863, 2019, pp. 269–292.

[21] Martínez-Tossas, L. A., Churchfield, M. J., and Meneveau, C., "A highly resolved large-eddy simulation of a wind turbine using an actuator line model with optimal body force projection," *Journal of Physics: Conference Series*, Vol. 753, IOP Publishing, 2016, p. 082014.

[22] Churchfield, M. J., Schreck, S. J., Martinez, L. A., Meneveau, C., and Spalart, P. R., "An advanced actuator line method for wind energy applications and beyond," *35th Wind Energy Symposium*, 2017, p. 1998.

[23] Kaimal, J., "Turbulence spectra, length scales and structure parameters in the stable surface layer," *Boundary-Layer Meteorology*, Vol. 4, No. 1-4, 1973, pp. 289–309.

[24] Cheynet, E., Jakobsen, J. B., and Obhrai, C., "Spectral characteristics of surface-layer turbulence in the North Sea," *Energy Procedia*, Vol. 137, 2017, pp. 414–427.

[25] Benedict, L., and Gould, R., "Towards better uncertainty estimates for turbulence statistics," *Experiments in Fluids*, Vol. 22, No. 2, 1996, pp. 129–136.

[26] Bartl, J., Mühle, F., Schottler, J., Sætran, L., Peinke, J., Adaramola, M., and Hölling, M., "Wind tunnel experiments on wind turbine wakes in yaw: effects of inflow turbulence and shear," *Wind Energy Science*, Vol. 3, No. 1, 2018, pp. 329–343.

[27] Williamson, C. H., "Vortex dynamics in the cylinder wake," *Annual review of fluid mechanics*, Vol. 28, No. 1, 1996, pp. 477–539.

[28] Achenbach, E., "Vortex shedding from spheres," *Journal of Fluid Mechanics*, Vol. 62, No. 2, 1974, pp. 209–221.

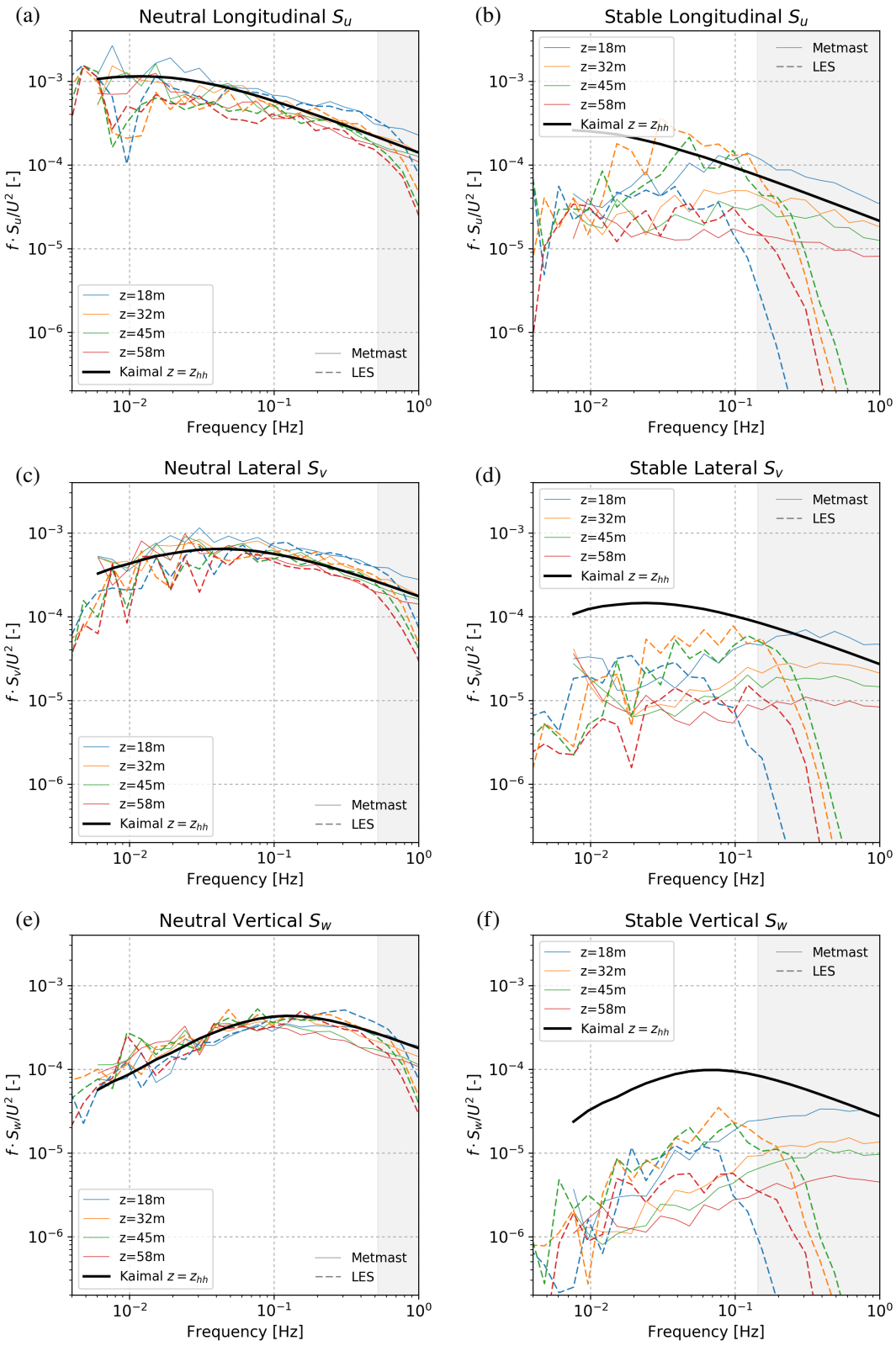

Fig. 4 Longitudinal S_u (a, b), Lateral S_v (c, d), and vertical S_w (e, f) inflow spectra for the neutral (a, c, e) and stable (b, d, f) ABL cases. The gray shaded regions correspond to frequencies beyond the maximum resolvable frequency f_{max} based on mesh spacings of Δ=1.25m and 2.5m for the neutral and stable cases, respectively.

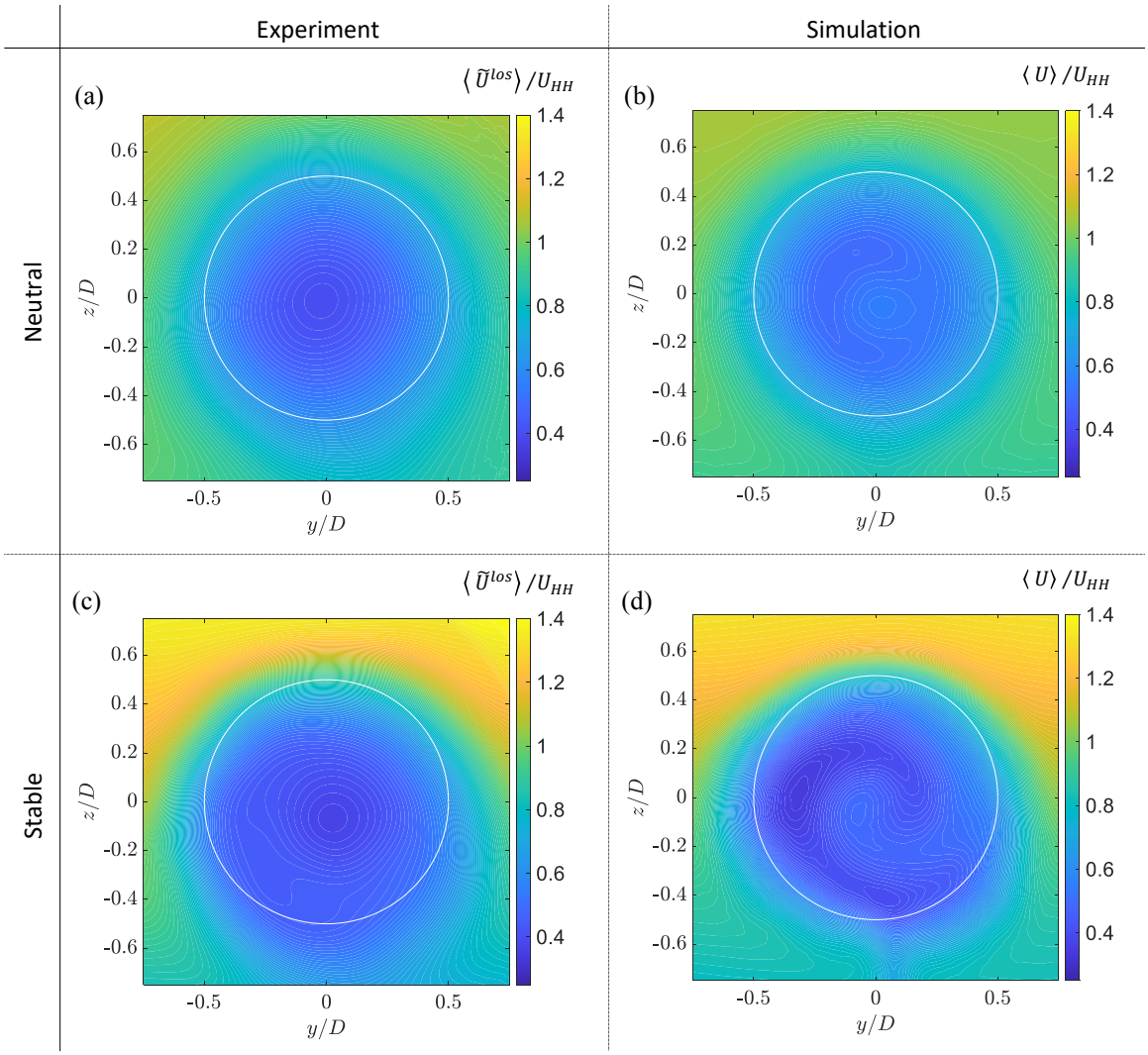

Fig. 5 Comparison of scaled values of wake velocities at the x=2.5D position in the meandering frame of reference. Plotted in (a) and (c) is the time-averaged spectral median of lidar line-of-sight velocity within the probe volume, $\langle \tilde{U}^{los} \rangle$. Plotted in (b) and (d) is time-averaged axial velocity, $\langle U \rangle$. All cases are normalized on the hub-height axial inflow velocity, U_{HH}. The viewing orientation is from behind the turbine and looking upstream.

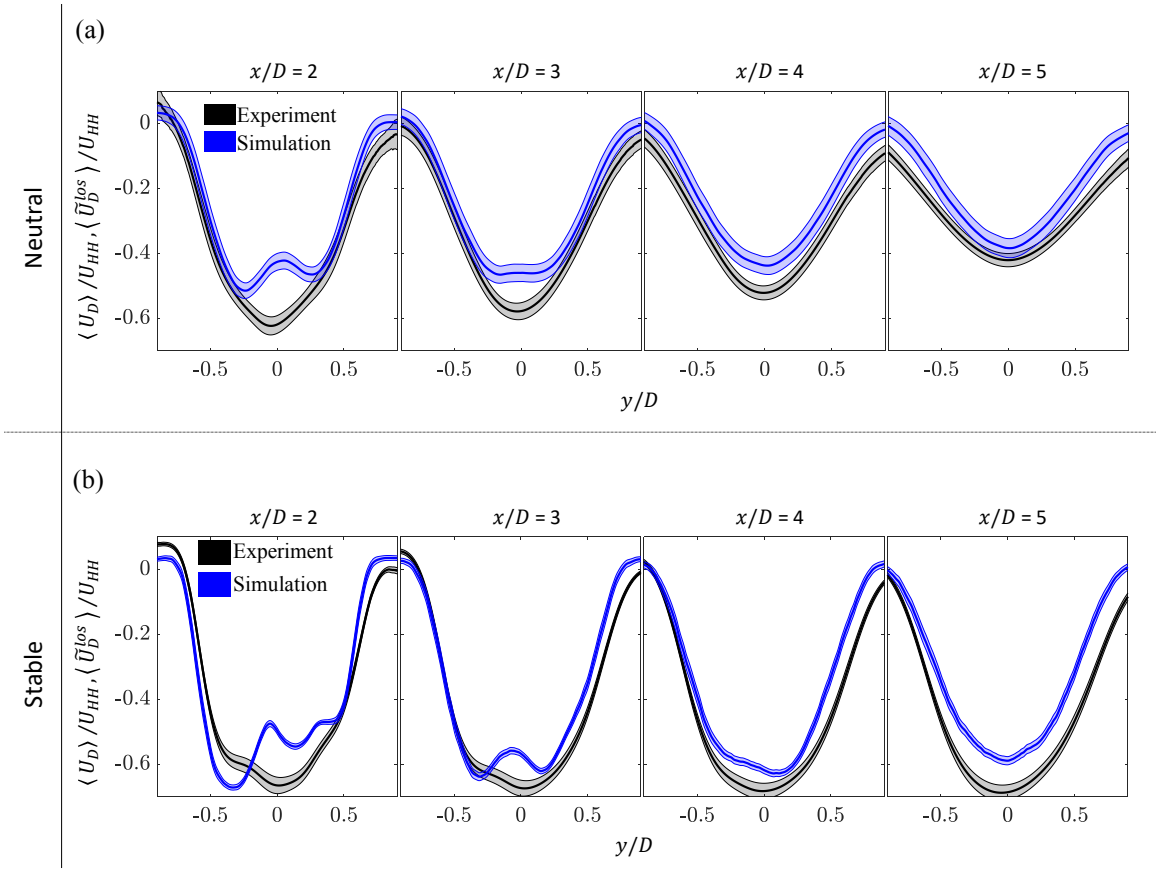

Fig. 6 Comparison of the streamwise evolution of the time-averaged wake velocity deficit in the meandering frame of reference from the lidar, $\langle \tilde{U}_D^{los} \rangle$, and the simulation, $\langle U_D \rangle$, at the vertical wake center for (a) the neutral case and (b) the stable case. Values are normalized on the hub-height axial inflow velocity, U_{HH}. The shaded regions indicate the 95% confidence of the standard error as calculated according to the formulas in Benedict and Gould [25] that are valid for turbulent quantities with any underlying probability distribution.

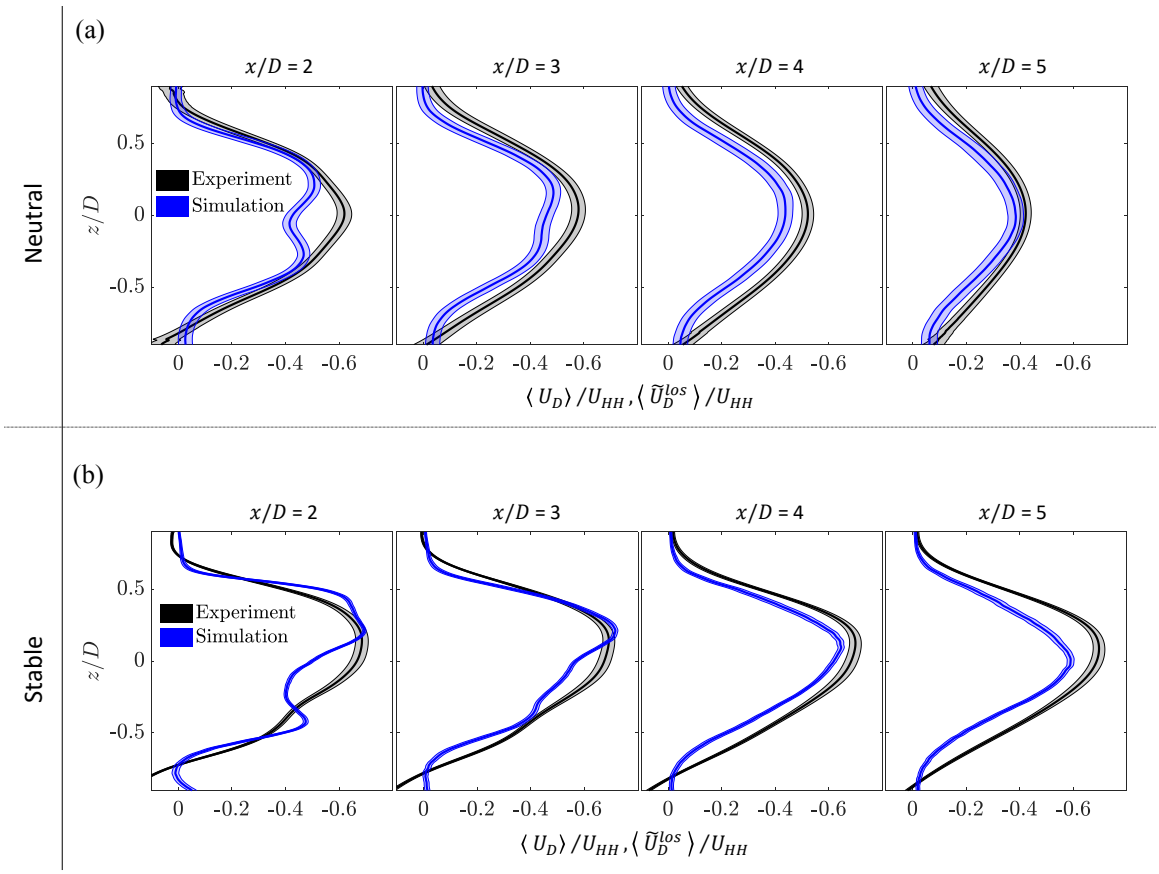

Fig. 7 Comparison of the streamwise evolution of the time-averaged wake velocity deficit in the meandering frame of reference from the lidar, $\langle \tilde{U}_D^{los} \rangle$, and the simulation, $\langle U_D \rangle$, at the horizontal wake center for (a) the neutral case and (b) the stable case. Values are normalized on the hub-height axial inflow velocity, U_{HH}. The shaded regions indicate the 95% confidence of the standard error as calculated according to the formulas in Benedict and Gould [25] that are valid for turbulent quantities with any underlying probability distribution.

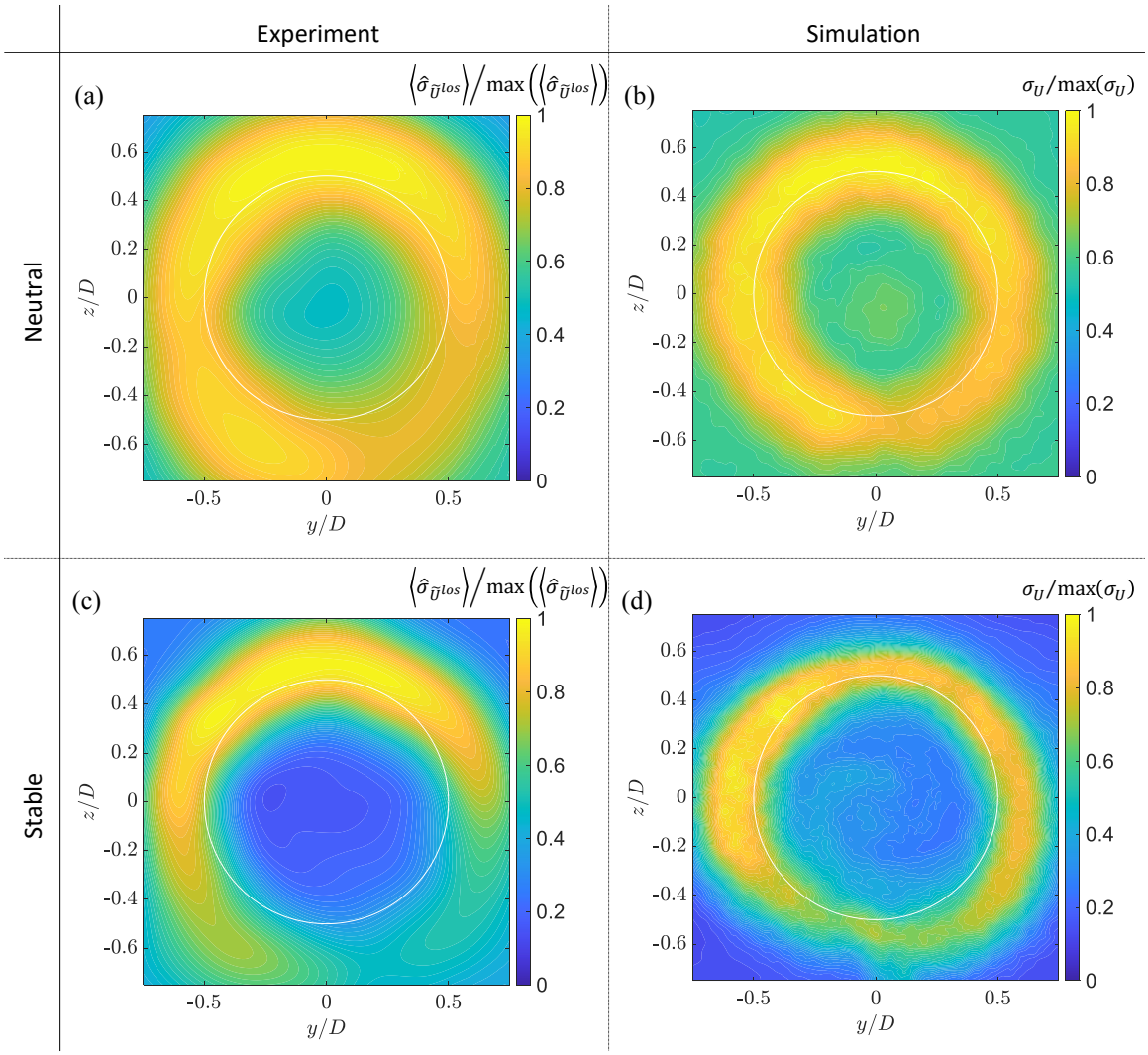

Fig. 8 Comparison of scaled values of wake fluctuations at the x=2.5D position in the meandering frame of reference. Plotted in (a) and (c) is the time-averaged spectral standard deviation of lidar line-of-sight velocity within the probe volume, $\langle\hat{\sigma}_{\tilde{U}^{los}}\rangle$. Plotted in (b) and (d) is the conventional standard deviation of axial velocity, σ_U. All cases are normalized on the maximum value within the respective plot windows. The viewing orientation is from behind the turbine and looking upstream.

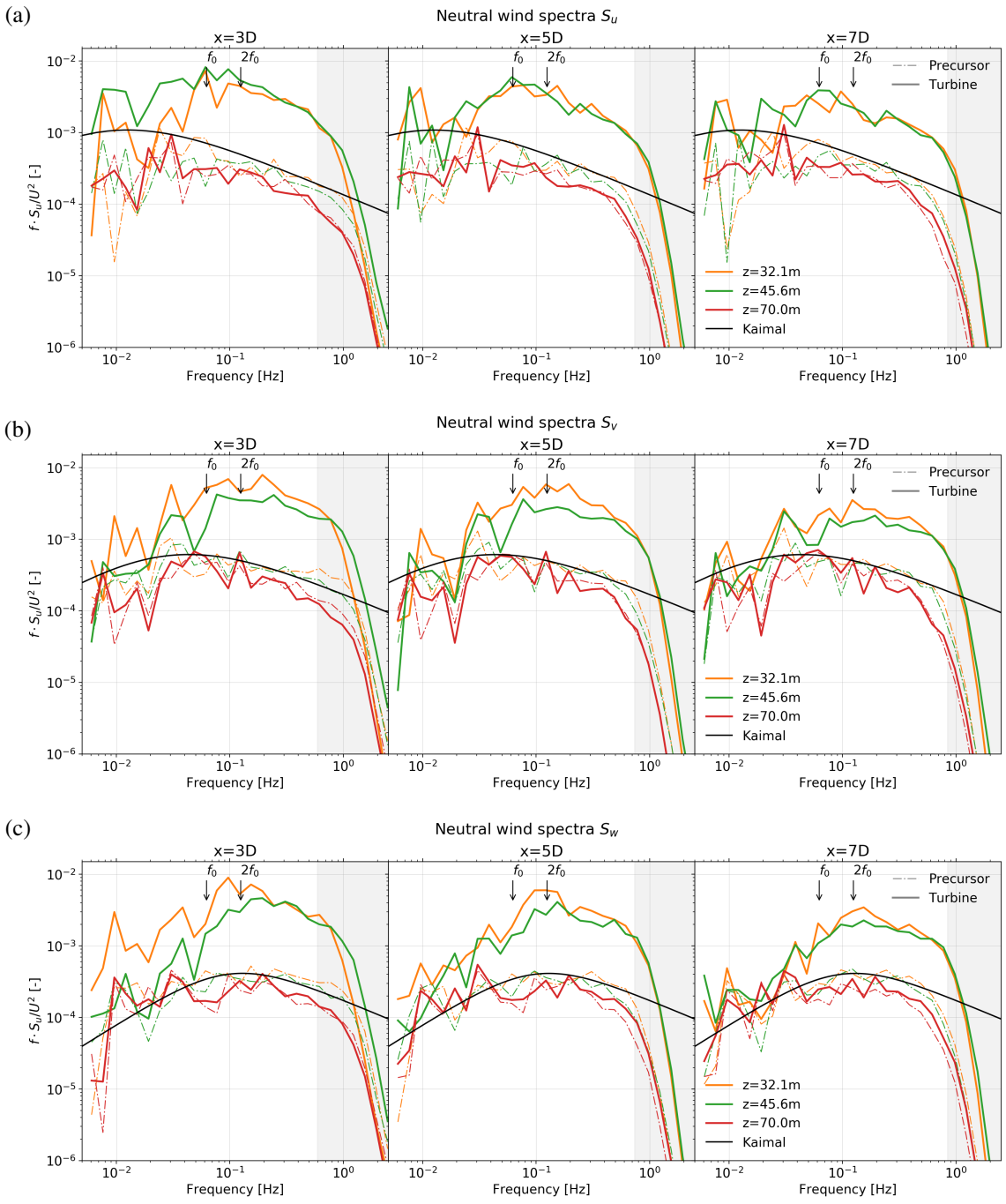

Fig. 9 Computed wind spectra for neutral ABL case, from both the precusor run (solid lines) and the turbine run (dashed lines): (a) longitudinal S_u, (b) lateral S_v, and (c) vertical S_w wind spectra components. The gray shaded regions correspond to frequencies beyond the maximum resolvable frequency f_{max}.

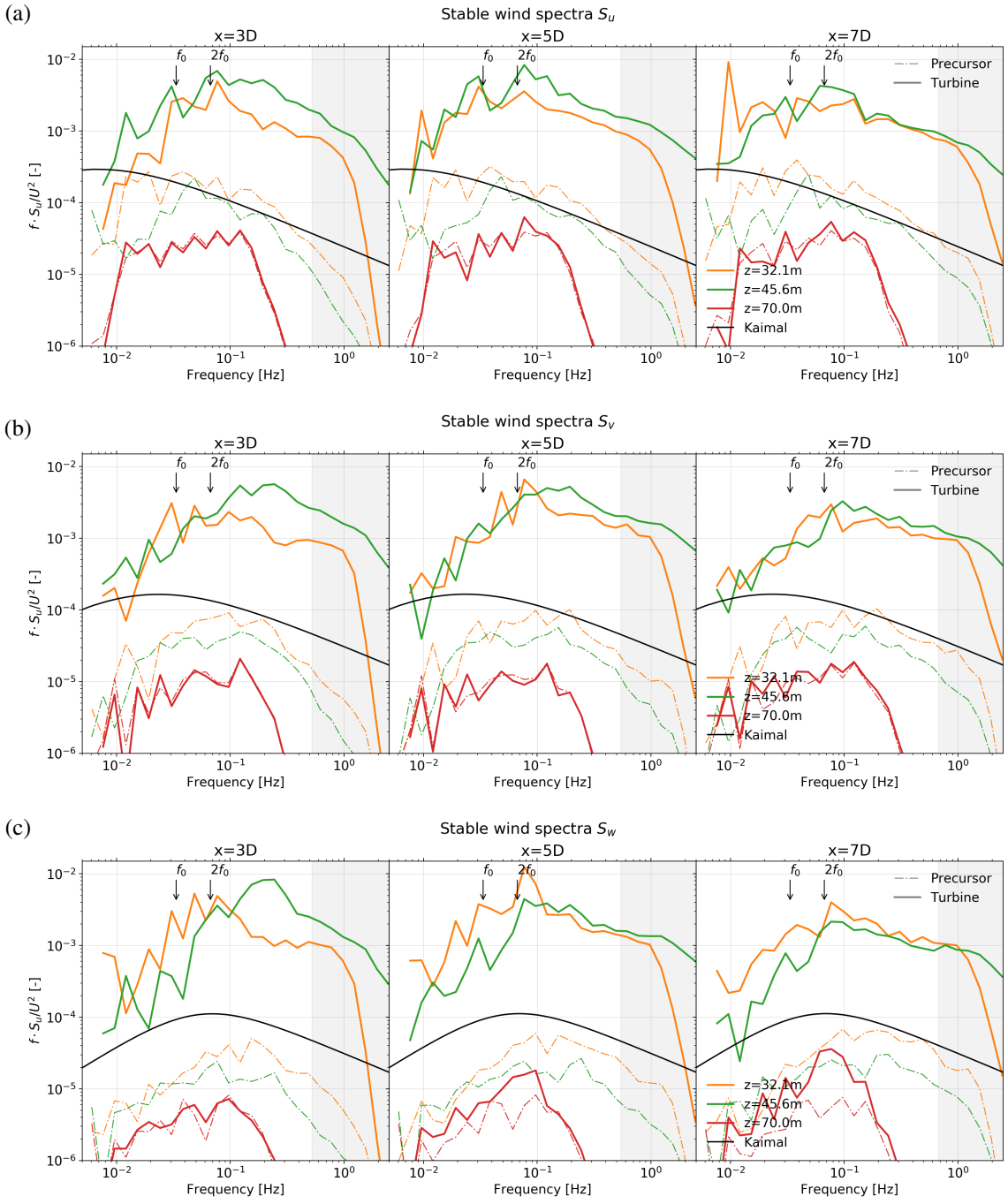

Fig. 10 Computed wind spectra for stable ABL, from both the precusor run (solid lines) and the turbine run (dashed lines): (a) longitudinal S_u, (b) lateral S_v, and (c) vertical S_w wind spectra components. The gray shaded regions correspond to frequencies beyond the maximum resolvable frequency f_{max}.

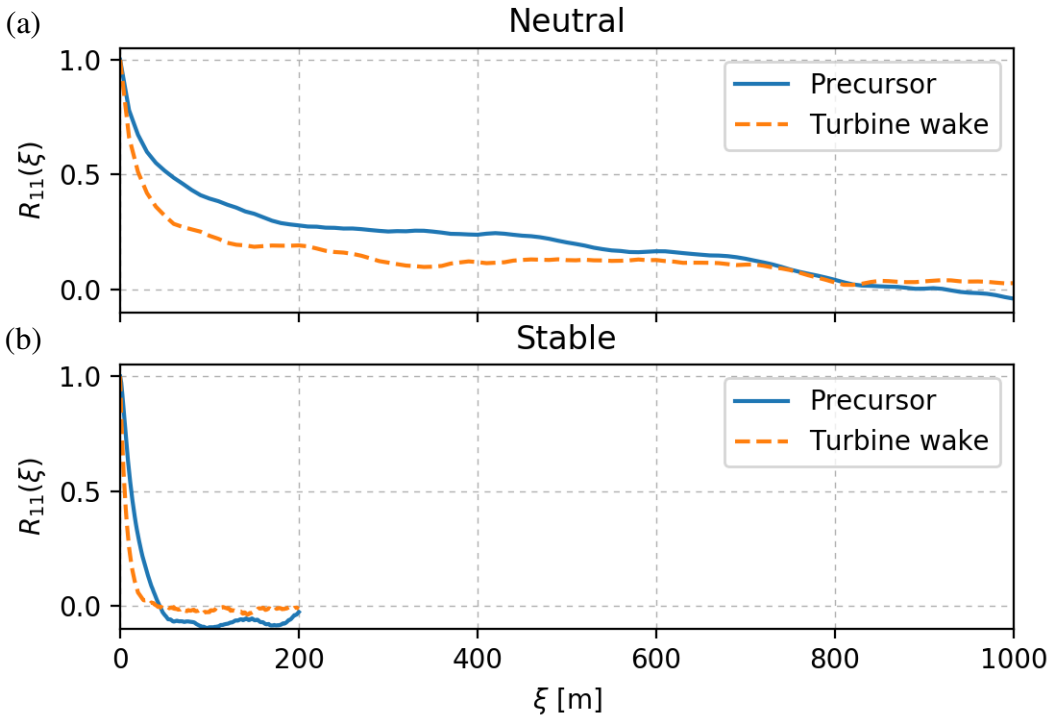

Fig. 11 Time-averaged, two-point turbulent correlation function $R_{11}(\xi)$ for the wake regions from the (a) neutral and (b) stable ABL cases. The correlation function for the precusor calculation alone is shown in solid lines, while the turbine calculation is shown in dashed lines.